Materials Research Express

PAPER • OPEN ACCESS

Development of inorganic-organic hybrid nanostructured material for H_2O_2 sensing application

To cite this article: Arvind Kumar *et al* 2020 *Mater. Res. Express* **7** 056201

Materials Research Express

PAPER

Development of inorganic-organic hybrid nanostructured material for H_2O_2 sensing application

Arvind Kumar[1], **Praveen Kumar Shahi**[2], **Amresh Bahadur**[1], **Sunil Kumar Singh**[3], **Rajiv Prakash**[4], **Ram Anjore Yadav**[1] and **Shyam Bahadur Rai**[1]

[1] Department of Physics, Banaras Hindu University, Varanasi, India
[2] Department of Physics, SPM Govt. Degree College (University of Allahabad), Allahabad, India
[3] Department of Physics, IIT (BHU), Varanasi, India
[4] School of Materials Science and Technology, IIT (BHU), Varanasi, India

E-mail: praveenkshahi@gmail.com

Keywords: hybrid nanoparticles, tunable emission, H_2O_2 sensor

Supplementary material for this article is available online

OPEN ACCESS

RECEIVED
10 January 2020

REVISED
19 March 2020

ACCEPTED FOR PUBLICATION
22 April 2020

PUBLISHED
4 May 2020

Abstract

An organic-inorganic hybrid nanoparticle (HNPs) composed of $Sm(TTA)_3Phen$, a coordination compound, and $NaY_{0.78}Er_{0.02}Yb_{0.20}F_4$, an upconversion nanoparticles (UCNPs), has been developed and used for H_2O_2 sensing application. Herein, $Sm(TTA)_3Phen$ absorbs ultraviolet (UV) light and gives fluorescence in yellow-red-near infrared (NIR) region. Whereas, the UCNPs absorb NIR radiations (980 nm) and consequently emit in green-red region through photon upconversion process. Two important optical phenomena are observed when HNPs are simultaneously excited with UV (266 nm) and NIR (980 nm) laser radiation- (i) an energy transfer from Sm^{3+} to Er^{3+} ions, and (ii) color tunable emission from red to green, if the power of 980 nm laser is varied. Further, the material is highly competent to sense H_2O_2 through fluorescence quenching of Sm^{3+} emission in presence of H_2O_2. The nature of quenching is conspicuously different for different concentration/volume range of H_2O_2. For lower volume range, the rate of decrease of emission/excitation intensity is linear, while for higher volume range the decay in intensity is exponential. The attained minimum detection limit for H_2O_2 is 2 μl, which is significant for sensing applications.

1. Introduction

Development of intense and tunable source of light is of fundamental importance in photonics for different technological applications. This permits one to carry out various measurements without disturbing the source and experimental setup. Such tunable light sources are frequently used in bio-medical sensing and industrial applications also [1–6]. A large variety of dye lasers, both in pulse and continuous mode, are already well known sources for tunable emission. However, these sources have limited tunability of only few Angstroms. Diode lasers also are the sources which are used for tunable emission but again they are tunable only upto 100 Angstroms. In this work, we have reported a hybrid material which gives us tunable radiation in between 500–700 nm spectral region both through normal fluoresce and photon upconversion process. Rare-earth (REs) are the active material for multi-color luminescence.

The unique and specific property of some trivalent REs (Er^{3+}, Tm^{3+}, Pr^{3+}, Tb^{3+} and Ho^{3+}) is to absorb two or more low energy photons via the involvement of real metastable states and thereafter consequently emit high energy photons. This process is termed as upconversion (UC) process [7–14]. The UC process is only feasible in REs. In addition to this, many of the REs have energy levels to absorb near infrared (NIR) photons perfectly matching with 980 nm diode laser [15–18]. One potential element in these REs is Yb^{3+} ion, which absorbs 980 nm photons very efficiently (more than ten times as compared to any other REs) due to large absorption cross-section. It may transfer its excitation energy to the resonant energy levels of other REs (e.g. Er^{3+}, Tm^{3+}, Pr^{3+}, Tb^{3+} and Ho^{3+}) and act as a sensitizer [19–21]. Thus, Yb^{3+} ions are used as co-dopant with other REs for

efficient UC luminescence. Further, optical properties of REs doped materials depend on local crystal field symmetry and hence on crystal structure, particle size and phase of the host material also [22–26]. In this work, $NaY_{0.78}Er_{0.02}Yb_{0.20}F_4$ is chosen for UC emission due to its highest quantum yield reported so far in the literature [27]. The emitted radiation of the active ion Er^{3+} lies mainly in green-red region.

REs based β-diketonates coordination compounds absorb ultraviolet (UV) and blue photons extensively through singlet state electronic transitions as due to presence of large number of π-electrons in the organic ligands. The absorbed energy of ligand in singlet state is transferred to its triplet states through intercross relaxation process. Thereafter, in the next step, it is resonantly transferred to the resonant energy states of REs, from where, intense and sharp emissions of REs are observed. This process of energy transfer is termed as sequential or cascade energy transfer [28–32]. In this work, a β-diketonate $Sm(TTA)_3Phen$ (STP) is chosen as it gives intense red emission of Sm^{3+} ion through normal photoluminescence process. The TTA and Phen ligands absorb UV-blue radiation via their singlet states (S_1 and S_2) and transfer it to their triplet states and finally to resonant and long lived energy states of Sm^{3+}. The excited Sm^{3+} gives one transition in green region (562 nm) and three transitions (609 nm, 646 nm and 714 nm) in yellow-red region in which emission peaking at 646 nm exhibits the highest intensity. Thus, the developed hybrid material may give emission ranging from green region to extreme red region (520–720 nm) under different source of excitations.

The unique photo-physical properties of HNPs further motivate us to extend this work for sensing of reactive oxygen species (ROS), particularly hydrogen peroxide (H_2O_2). Hydrogen peroxide (H_2O_2) is one of the principal members of reactive oxygen species (ROS) and affects biological systems significantly, used in industries, pharmaceuticals and other fields, etc [33–39]. H_2O_2 is also present in atmosphere in small content. In addition to this, H_2O_2 is also a byproduct of the reactions catalyzed by large number of oxidase enzymes, where the oxidase enzyme converts H_2O_2 into water and oxygen [37]. In past three decades, different elegant spectroscopic, electrochemical and enzymatic approach based techniques have been used for the detection of H_2O_2 [38–44].

In this work, the H_2O_2 sensing application has been carried out using spectroscopic (fluorescence) technique, in which the fluorescence intensity is measured and plotted as a function of different volume/content of H_2O_2. The H_2O_2 volume dependent variation in luminescence intensity, linear for low volume and exponential for high volume, is unique by any fluorophore and first time reported in this work.

2. Materials and methods

2.1. Materials

Erbium oxide (99.999%), yttrium oxide (99.99%), ytterbium oxide (99.998%), samarium oxide (99.99%), 2-theonyltrifluoroacetone (TTA) (99.9%), 1–10 phenonthroline (Phen) (99%) and ODE (90%) are purchased from Alfa Aesar. While, methanol, sodium hydroxide, ammonium fluoride, diethyl ether AR, cyclohexane GR and oleic acid were purchased from Fisher scientific. Ethanol was Purchas from Merck Germany. These chemicals are used as such for synthesis without further processing or purification.

2.2. Synthesis

2.2.1. Synthesis of $NaY_{0.78}Er_{0.02}Yb_{0.2}F_4$

The synthesis of Er^{3+} and Yb^{3+} doped $NaYF_4$ UCNPs were carried out by using thermal decomposition technique. The detailed synthesis process is reported in our earlier reports [45, 46].

2.2.2. Synthesis of $Sm(TTA)_3Phen$ coordination compound

The synthesis of STP was carried out using solution cast technique [29]. The $SmCl_3.6H_2O$ was prepared by dissolving samarium oxide into minimal amount of concentrated hydrochloric acid. TTA (6 mmoles), Phen (2 mmoles) and 8 ml of 1N solution of NaOH were dissolved in ethanol and a homogeneous solution was prepared. (2mmoles) of $SmCl_3.6H_2O$ was dissolved in 10 ml of distilled water and then added to the former solution with a constant stirring for better reaction. A white color precipitate of $Sm(TTA)_3Phen$ complex was formed. The precipitate was further washed with distilled water for four times and dried in oven at 40 °C.

2.2.3. Synthesis of hybrid nanophosphor (HNPs)

The $Sm(TTA)_3Phen$ and $NaY_{0.78}Er_{0.02}Yb_{0.20}F_4$ were mixed in cyclohexane in equal molar ratio under a constant stirring for five hours. The mixture is then centrifuged for 1 h in order to get well developed HNPs. The HNPs was then dried in oven at 40 °C for ten hours.

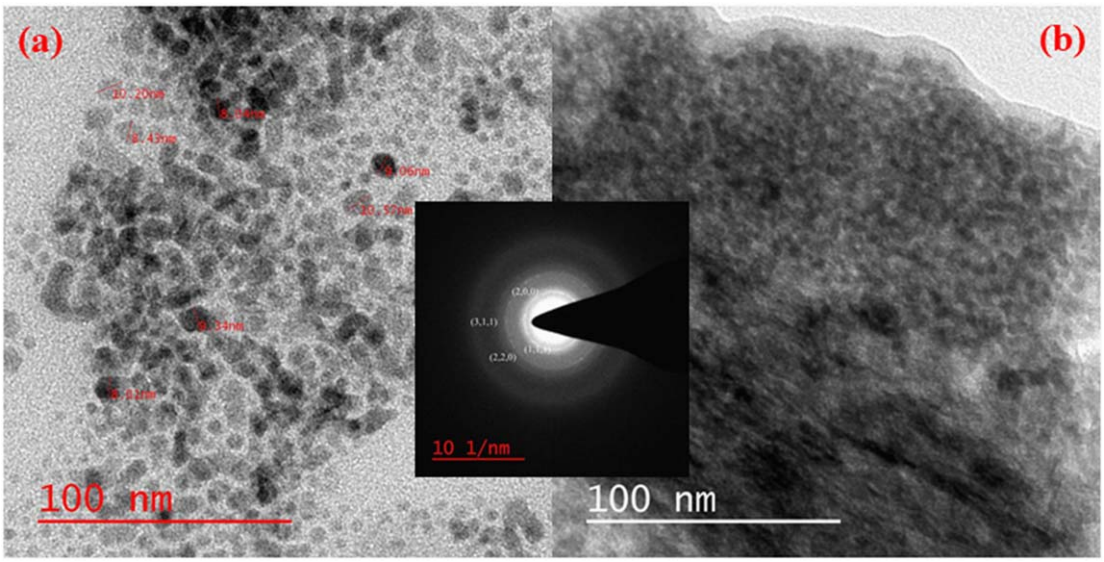

Figure 1. (a) TEM image of UCNPs at 100 nm scale bar (b) TEM image of HNPs at 100 nm scale bar. SAED pattern of UCNPs is shown in inset.

2.3. Characterization

X-ray diffraction (XRD) patterns of UCNPs, STP, and HNPs were measured using X-ray diffractometer (Model No: Miniflex-II, Rigaku, Japan) with CuK_{α} radiation $\lambda = 1.5406$Å. The transmission electron microscope (TEM) and the high resolution TEM images were recorded using an FEI, Tecnai G^2, S-Twin instrument operating at 200 KV. Fourier transform infrared (FTIR) spectra were recorded using Perkin-Elmer frontier FTIR spectrometer-35 in the spectral range 400-4000 cm^{-1}. The UV–vis-NIR absorption spectra of these samples were recorded in the range 200-1100 nm using Perkin Elmer, Lambda 750 spectrophotometer. Photoluminescence excitation, emission, lifetime measurements were performed by fluorescence spectrometer (Model no: FL-3-11 Horiba Jobin Yvon) equipped with 25 W pulsed xenon (Xe) lamp, 450 W CW Xe lamp and PMT detector (model No: FL-1073). The UC emission spectra were recorded by using 980 nm (CW, 2W, power tunable) diode laser as an excitation source and a dispersing monochromator (Model no: iHR320, Horiba Jobin Yvon) attached with a PMT (Model no.1424M) as a detector.

3. Results and discussion

3.1. Transmission electron microscopy (TEM) and x-ray diffraction (XRD) analysis

TEM measurements of UCNPs and HNPs are carried out to observe the microstructure and particle size. Figure 1(a) shows the TEM image of UCNPs at 100 nm scale bar. Average size of the particles is found in the range of 10–15 nm. Figure 1(b) shows the TEM image of HNPs and it clearly depicts that, the UCNPs are fairly dispersed in STP and forms a sheet like structure. The inset of figure 1(a) shows the selected area electron diffraction (SAED) pattern of UCNPs. The SAED pattern shows four rings and these rings corresponds to (1,1,1), (2,0,0), (2,2,0) and (3,1,1) planes of $NaYF_4$ crystal in face centered cubic phase. Phase of the NPs have been further verified using XRD analysis also.

Figure S1 is available online at stacks.iop.org/MRX/7/056201/mmedia shows the XRD pattern of UCNPs, STP and HNPs. The XRD pattern of UCNPs matches well with the face centered cubic phase of $NaYF_4$ crystal with lattice parameters $a = b = c = 5.448$ Å (JCPDF file no. 06-0342). The calculated d-spacing from SAED pattern matches well for the inter-planner separation between the (1,1,1), (2,0,0), (2,2,0) and (3,1,1) planes with JCPDF file no. (06-0342). Crystallite size has also been calculated by using Debye Scherer's formula [47, 48]. Average crystallite size is found to be 7.9 nm which is in accordance with TEM measurements.

3.2. Absorption spectra of solid UCNPs, STP and HNPs

Absorption spectra of solid UCNPs, STP and HNPs are recorded in the range from 200-1000 nm and are shown in figure 2. The absorption spectrum of UCNPs shows no peaks in UV and visible region, although a weak absorption band is observed in NIR region around 980 nm (as shown in the inset of figure 2). The host absorption band due to $NaYF_4$ lies at higher energy while the peaks due to Er^{3+} do not appear due to low absorption cross-section. On the other hand, the absorption spectrum of STP shows two intense absorption

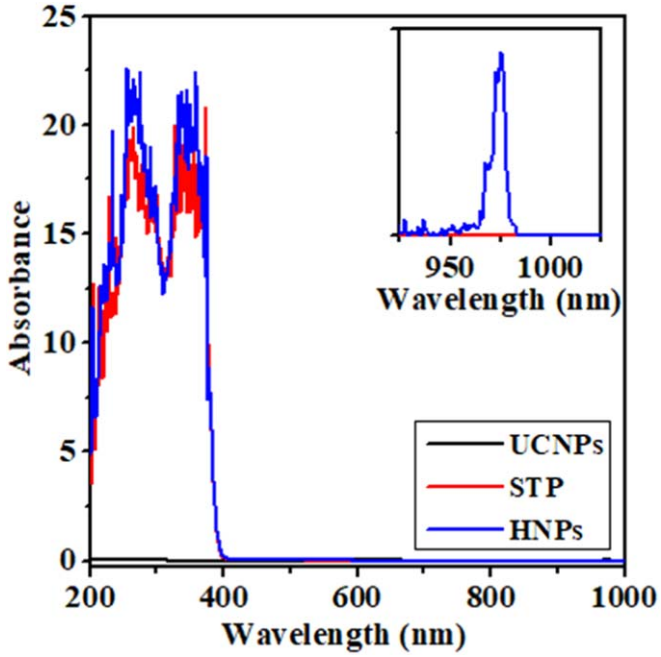

Figure 2. Absorption spectra of UCNPs, STP and HNPs. Absorption spectrum due to Yb^{3+} ($^2F_{7/2} \rightarrow {}^2F_{5/2}$) of UCNPs and HNPs in NIR region is shown in the inset.

bands peaking at 273 nm and 390 nm. The intense absorption band at 390 nm is due to $\pi \rightarrow \pi^*$ electronic transition ($S_0 \rightarrow S_1$) of TTA while broad absorption band at 273 nm probably arises due to overlapping of $\pi \rightarrow \pi^*$ electronic transition ($S_0 \rightarrow S_1$) of phen and n $\rightarrow \pi^*$ electronic transition ($S_0 \rightarrow S_2$) of TTA [28].

The absorption spectrum of HNPs contains peaks both due to UCNPs and STP, and shows strong UV absorption due to STP and weak NIR absorption due to UCNPs. The absorption intensity of bands remains almost unaltered as compared with STP and UCNPs. This also suggests that, both the constituent in HNPs are not interacting strongly. So, it is expected that the constituent particles of HNPs are entangled through weak forces, like Vander wall interaction, similar to composite materials [45, 46].

3.3. Photo-physics, decay dynamics and energy transfer in coordination compound STP

Figure 3(a) shows emission spectra of STP and HNPs under 390 nm excitations. The emission spectrum of STP on excitation with 390 nm radiation shows emission bands at 562, 609, 646 and 706 nm which are assigned due to $^4G_{5/2} \rightarrow {}^6H_{5/2,}$ $^4G_{5/2} \rightarrow {}^6H_{7/2}$, $^4G_{5/2} \rightarrow {}^6H_{9/2}$ and $^4G_{5/2} \rightarrow {}^6H_{11/2}$ transitions of Sm^{3+} ion, respectively. Among all these transitions, $^4G_{5/2} \rightarrow {}^6H_{9/2}$ transition peaking at 646 nm is most intense and sharp which is responsible for the characteristic red emission of STP complex [29]. The excited Sm^{3+} ions in different states relax down to $^4G_{5/2}$ metastable state by non-radiative relaxation process. The emission intensity is maximum under the 390 nm excitation due to combined effect of energy transfer from ligand to Sm^{3+} ion and a direct excitation of Sm^{3+} ions. The spectral lines also show Stark's components which indicate that Sm^{3+} ions are surrounded by ligand. The similar emission spectrum is observed in HNPs also, only emission intensity varies slightly.

The decay curve of $^4G_{5/2} \rightarrow {}^6H_{9/2}$ transition corresponding to 390 nm excitation for STP and HNPs are shown in figures 3(b), (c). The lifetime of $^4G_{5/2}$ levels of Sm^{3+} ion in STP and in HNPs are found to be 66 μs and 71μs, respectively. The lifetime in HNPs is slightly higher. It may be due to weak Vander wall interaction and reduction in high frequency vibrational bands (figure S2 shows the FTIR spectra of UCNPs, STP and HNPs. The detailed analysis is mentioned in supplementary section). The emission spectra and the lifetime can be explained by using the partial energy level diagram shown in figure 4. In coordination compounds, the energy transfer from organic ligands to lanthanide ions is termed as 'antenna effect'.

In the present case, energy is transferred from TTA and phen ligands to Sm^{3+} ions [28]. It is obvious from figure 4 that the UV photons are initially absorbed by TTA and Phen through their singlet electronic states. The energy transfer from ligand to Sm^{3+} ions may occur in different ways- (i) electronically excited level of phen (S_1) is very close to S_2 state of TTA. Thus a transfer of energy from phen singlet S_1 to TTA singlet S_2 may occur. The energy from S_2 level of TTA subsequently relaxes to S_1 energy level of TTA via internal conversion (IC). The TTA then may transfer its energy to Sm^{3+} ions (via singlet level or triplet level of TTA to Sm^{3+} ion), (ii) It is also possible that, phen is excited to singlet S_1 via $S_0 \rightarrow S_1$ absorption and then relaxes nonradiatively to its triplet

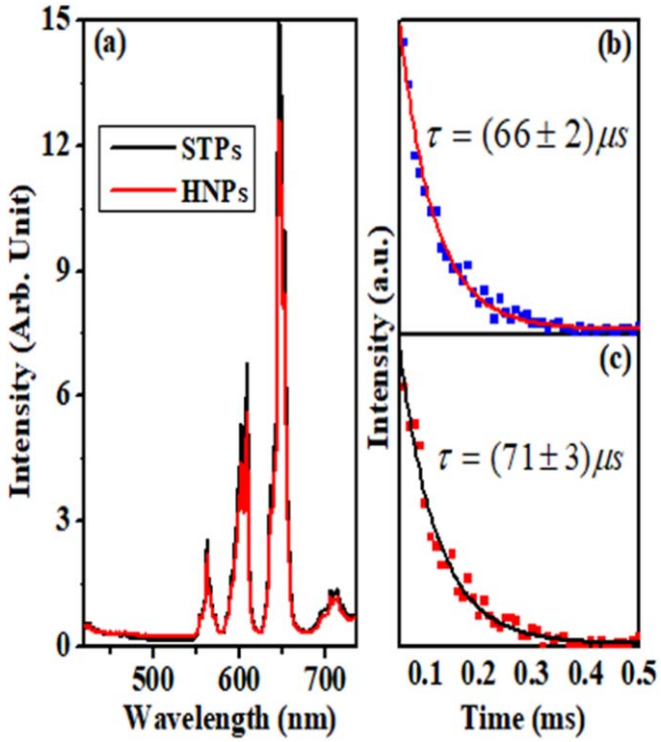

Figure 3. (a) Emission spectra of STP and HNPs under 390 nm excitation, and (b), (c) Lifetime measurements of STP and HNPs for the emission line at 646 nm ($\lambda_{exc} = 390$ nm) corresponding to $^4G_{5/2} \rightarrow {}^6H_{9/2}$ transition of Sm^{3+}.

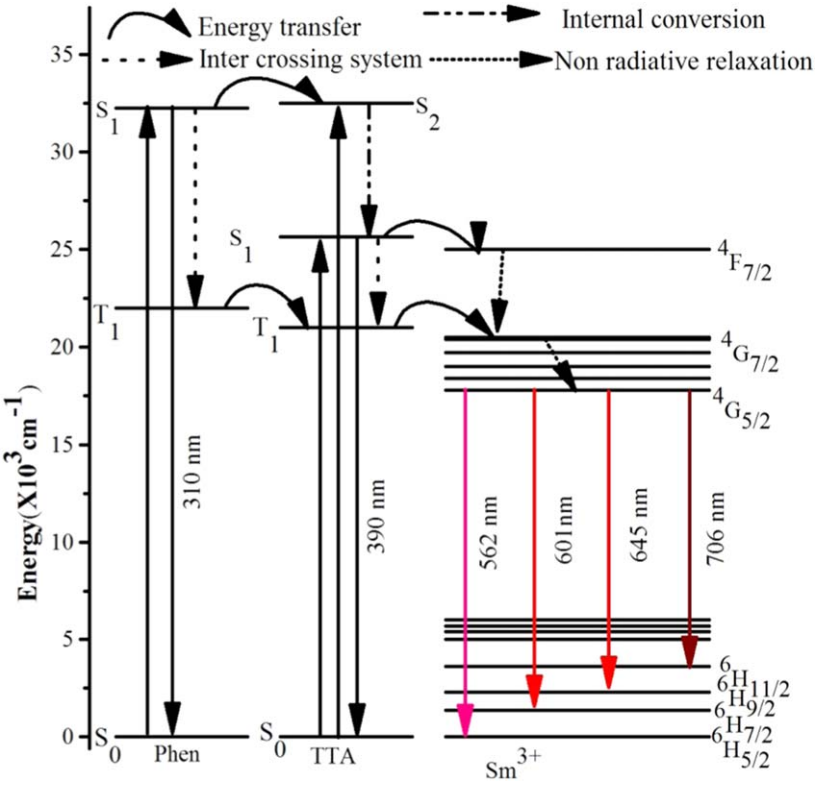

Figure 4. Partial energy level diagram showing possible pathways involved in energy transfer between ligands (Phen and TTA), ligands to Sm^{3+} and transitions of Sm^{3+} ion in STP complex.

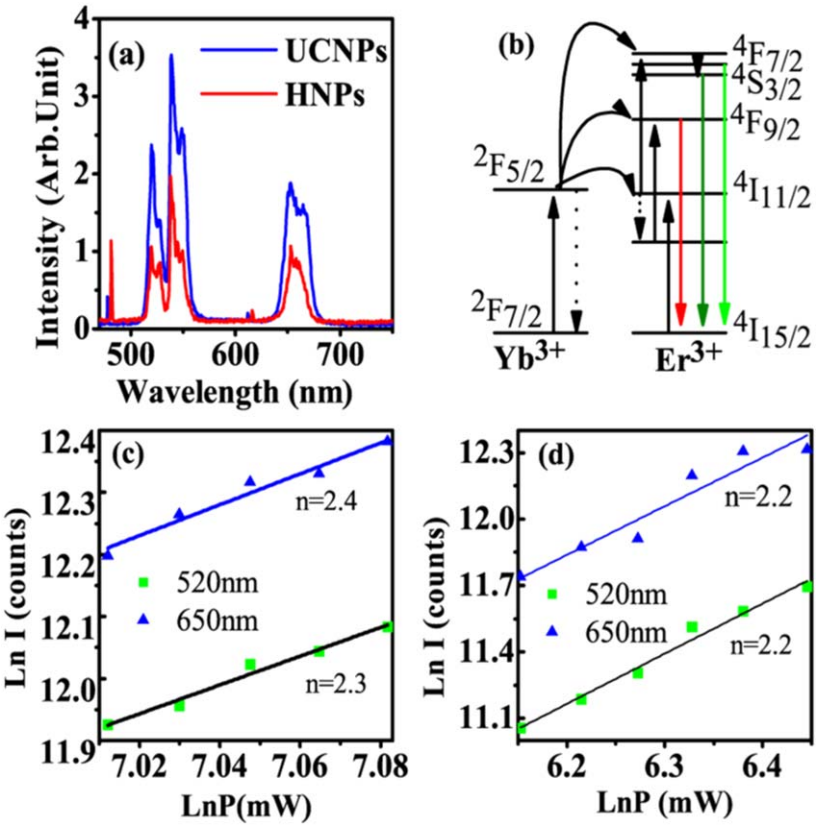

Figure 5. (a) Upconversion emission spectra of UCNPs and HNPs. (b) Energy level diagram of Er^{3+} and Yb^{3+} explaining upconversion process. (c) Power dependence plot for different transitions of UCNPs. (d) Power dependence plot of HNPs.

state. The triplet level of phen transfer its energy to triplet level of TTA and finally to Sm^{3+} ions. The ligand TTA excited to S_1 may also transfer its energy to triplet of TTA, via inter-crossing system (ISC). Then the TTA triplet level finally transfers the energy to Sm^{3+} ions. Thereon the different transitions of Sm^{3+} are observed.

3.4. Upconversion emission

The UC emission has been monitored by using 2W tunable continuous wave 980 nm diode laser as a source of excitation. It is found that STP gives no UC emission. On the other hand, UCNPs and HNPs give intense UC emission. The upconversion emission spectra of UCNPs and HNPs are shown in figure 5(a). The emission bands are observed at 521, 540 and 649 nm corresponding to $^2H_{11/2} \rightarrow {}^4I_{15/2}$, $^4S_{3/2} \rightarrow {}^4I_{15/2}$ and $^4F_{9/2} \rightarrow {}^4I_{15/2}$ transitions of Er^{3+} ions, respectively. The red emission at 650 nm is relatively weak than the green emission bands. It is important to notice that, all the emission bands show Stark components which suggest a high electric field of host material on the Er^{3+} ions. The energy levels of the sensitizer Yb^{3+}, activator Er^{3+} and upconversion mechanism is shown in figure 5(b).

There are two processes responsible for UC emission, excited state absorption (ESA) of Er^{3+} and energy transfer from Yb^{3+} to Er^{3+} ion. In ESA process, Er^{3+} ions absorb pump photons (980 nm) and are promoted to excited state $^4I_{11/2}$. Some of the excited Er^{3+} ions in $^4I_{11/2}$ level may relax and populate low lying $^4I_{13/2}$ level. Now, population in $^4I_{13/2}$, $^4I_{11/2}$ absorbs another photon and are promoted to $^4F_{9/2}$ and $^4F_{7/2}$ levels in presence of laser excitation. The ions in the $^4F_{7/2}$ excited state further relax nonradiatively to the metastable states $^2H_{11/2}$ and $^4S_{3/2}$ which ultimately decay to ground state and gives green emission. Similarly, the red transition is observed from $^4F_{9/2}$ level. The levels $^4I_{11/2}$, $^4F_{7/2}$ are also populated from an energy transfer of Yb^{3+} to Er^{3+}, as shown on figure.

The number of photons involved in a particular UC luminescence process can be given a.s [49, 50].

$$I = CP^n. \quad (1)$$

Where I_{uc} is the UC luminescence intensity, C is the constant related to material; P is the pump power of the laser and n is the number of photons involved to produce the UC luminescence. The ln-ln plot of UC emission intensity versus pump power of UCNPs and HNPs are shown in figures 5(c) and (d), respectively. The calculated values of n are found to be 2.3 and 2.4 corresponding to 520 nm and 650 nm emissions for UCNPs. While in

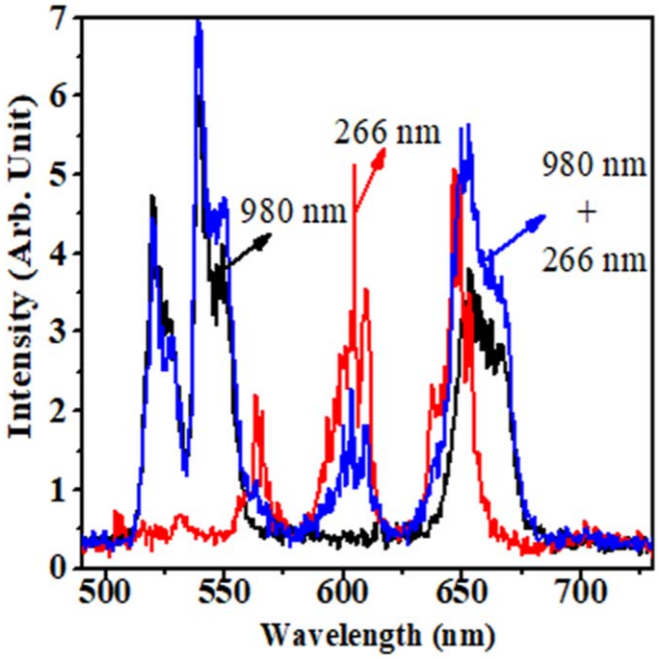

Figure 6. Emission spectra of the HNPs monitored by exciting the sample with 980 nm and 266 nm individually and with 266 nm + 980 nm simultaneously.

HNPs, the value of n is 2.3 and 2.2 for 520 nm and 650 nm emissions, respectively. This also supports our proposed mechanism of two photon upconversion process for green and red emission.

3.5. Simultaneous excitation of Sm^{3+} and Er^{3+}

The emission spectrum of HNPs was monitored by focusing two excitation (266 nm and 980 nm, both by laser source) collinearly on the sample simultaneously also. Figure 6 shows the emission spectra of the HNPs monitored by exciting the sample with 980 nm and 266 nm individually and then simultaneously. The UC spectrum ($\lambda_{exc} = 980$ nm) gives characteristic emission bands of Er^{3+} as explained above. Similarly, photoluminescence emission spectrum ($\lambda_{exc} = 266$ nm) gives characteristic emission bands of Sm^{3+}. However, the emission spectra monitored with 266 nm + 980 nm excitations show two new optical effects- (i) an energy transfer from Sm^{3+} to Er^{3+}, and (ii) a strong and broad red emission at about 650 nm.

The first effect is based on the fact that, the emission intensity of Er^{3+} is increasing while the emission intensity of Sm^{3+} is decreasing upon excitation of HNPs with two lasers simultaneously. Particularly, emission intensity of $^4S_{3/2} \rightarrow {}^4I_{15/2}$ transition of Er^{3+} (at 540 nm) increases while emission intensities of $^4G_{5/2} \rightarrow {}^6H_{5/2}$ and $^4G_{5/2} \rightarrow {}^6H_{7/2}$ transitions of Sm^{3+} (at 562 nm and 609 nm, respectively) decrease. In fact emission intensity due to $^4G_{5/2} \rightarrow {}^6H_{5/2}$ transition (at 562 nm) almost diminishes. The $^4G_{7/2}$ state of Sm^{3+} is close with the $^4F_{7/2}$ level of Er^{3+}, thus the energy transfer from Sm^{3+} to Er^{3+} seems possible (as shown in figure 7). Further, the second effect is observed in the view of combined intensity of emission due to $^4G_{5/2} \rightarrow {}^6H_{9/2}$ transition of Sm^{3+} and $^4F_{9/2} \rightarrow {}^4I_{15/2}$ transition of Er^{3+}. Thus, the strong red emission is due to the overlapped emission band of both Sm^{3+} and Er^{3+} under dual excitation.

The hybrid material promises the color tunability in the range from 520 nm to 660 nm with laser excitation power. The CIE diagram shown in figure 8 indicates that the HNPs shows the pure red emission under 266 nm exciation. Now, if we increase the power of 980 nm diode laser (keeping 266 nm laser power fix) the HNPs shows the tunable colour from pure red, yellowish to pure green color [51, 52]. Variation of color coordinate with different laser power is given in table 1.

3.6. Application of HNPs as sensor for H_2O_2

In order to realize a sensor for H_2O_2, firstly, the HNPs were dissolved in cyclohexane keeping concentration of solution maintained at 10^{-5} M. Then, different volume/content (starting from 2 μl) of H_2O_2 (in step of 2μl, upto 58μl) were added to 10 ml of HNPs solution. Presence of H_2O_2 in HNPs highly affects both excitation as well as emission intensity of Sm^{3+} and thus both may be used as parameter to probe the sensitivity. Figure 9 shows excitation spectra ($\lambda_{ems} = 645$ nm) of HNPs as a function of H_2O_2 content. It clearly depicts that, intensity of the excitation band decreases on increasing the contents of H_2O_2. Plot of excitation intensity versus H_2O_2 contents shows two clearly distinct patterns. The first pattern is observed for upto 28 μl content of H_2O_2

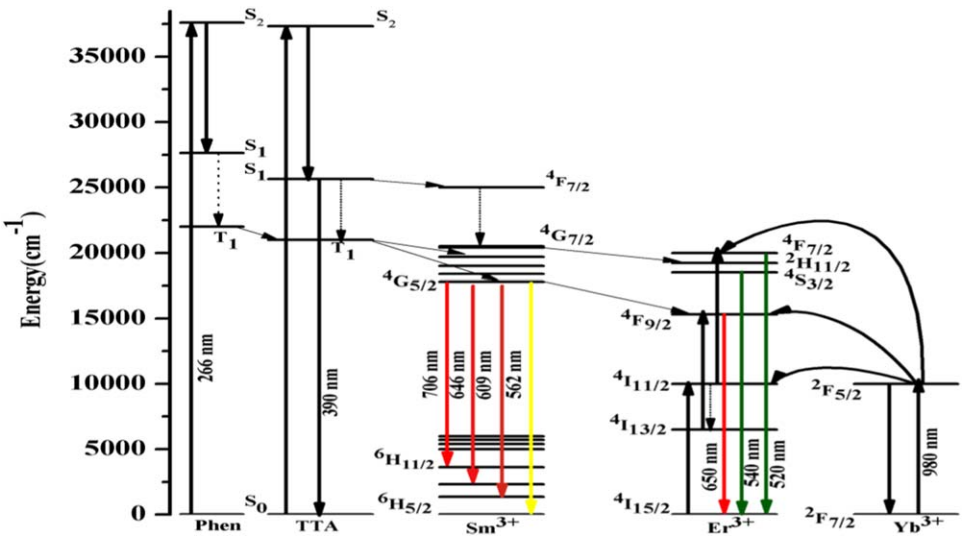

Figure 7. Partial energy level diagram showing the different pathways for energy transfer from Sm^{3+} (of coordination compound STP) to Er^{3+} ions (of UCNPs) in HNPs.

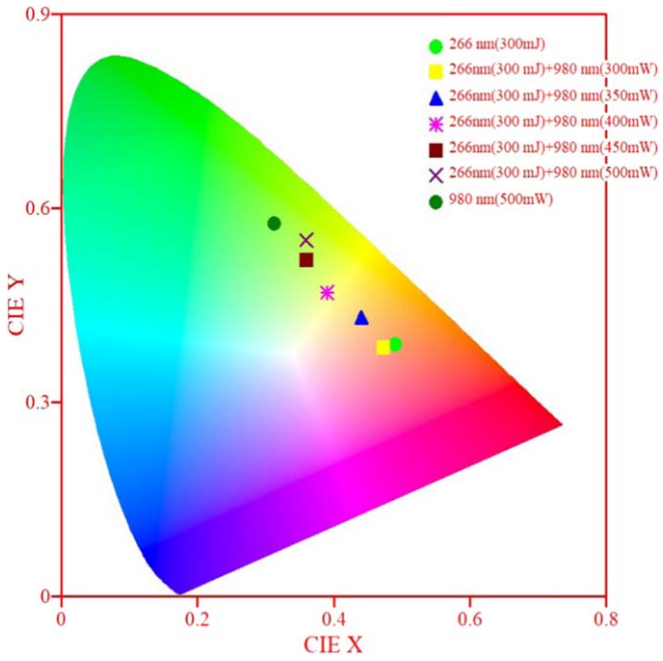

Figure 8. CIE chromaticity diagram for HNPs under dual excitation (266 nm + 980 nm) is showing a variation of color coordinates under the variation of 980 nm laser input power.

(figure 9(a)) that shows a minimum of 2 μl of H_2O_2 content can be sensed with resolved excitation intensity. The rate of intensity drop in this regime is slow and it shows almost a linear behavior (figure 9(c)). The second type of pattern is observed for the H_2O_2 content beyond 28 μl upto 58 μl (figure 9(b)). The rate of intensity drop in this content range is very fast and shows exponential decay behavior (figure 9(d)).

The measurement was repeated and the result remains unaltered. The sensitivity (s) of linear region can be calculated using the slope of the straight line and can be expressed as-

$$s = \frac{\Delta I}{I.\Delta c}. \tag{2}$$

Where, ΔI is the change in intensity, I is the intensity at zero μl content of H_2O_2 and Δc is the change in the volume of H_2O_2. Sensitivity for linear part thus calculated is found to be 2.95% signal decrease per μl of H_2O_2 addition, which is quite high for sensing purpose.

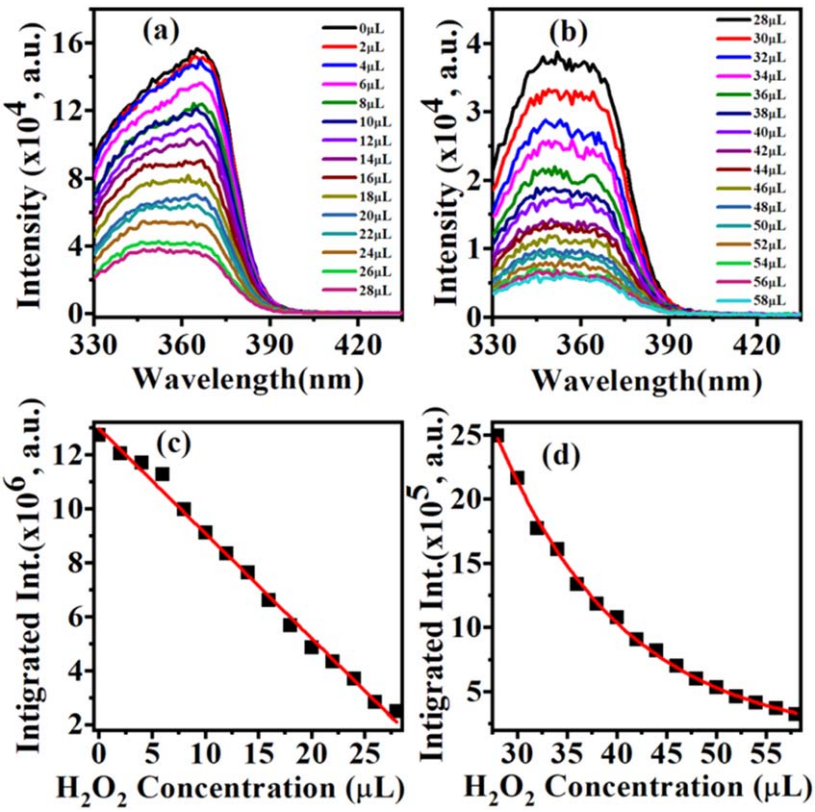

Figure 9. Excitation spectra (for $\lambda_{ems} = 645$ nm of Sm^{3+}) of HNPs as a function of H_2O_2 content- (a) H_2O_2 content in range 0–28 μl, and (b) H_2O_2 content in range 28–58 μl. Similarly, excitation intensity plot as a function of H_2O_2 content showing- (c) a linear behavior for H_2O_2 content in range 0–28 μl, and (d) exponential behavior for H_2O_2 content in range 28–58 μl.

Table 1. Variation of CIE color coordinates under the variation of 980 nm laser power.

S.No.	laser power (mJ) $\lambda_{exc} = 266$ nm	laser power (mW) $\lambda_{exc} = 980$ nm	Color co-ordinate (X, Y)
1.	300	0	(0.49,0.39)
2.	300	300	(0.47,0.38)
3.	300	350	(0.44,0.43)
4.	300	400	(0.40,0.48)
5.	300	450	(0.36,0.52)
6.	300	500	(0.36,0.55)
7.	0	500	(0.31,0.58)

Figure 10(a) shows the emission spectra ($\lambda_{exc} = 368$ nm) of HNPs as a function of H_2O_2 content. Fluorescence intensity of all the emission bands (562 nm, 602 nm and 645 nm) of Sm^{3+} gradually decreases and at higher contents (>42 μl), all the emission band almost disappear. This suggests a quenching of emission intensity due to addition of H_2O_2. Two reasons for this type of quenching are possible. The first mechanism proposes that, H_2O_2 may heterolytically break into H_2O and O_2 on UV light exposure (368 nm excitation). Since, vibrational frequencies of H_2O is very high (1885 cm^{-1} for H-O-H bending mode and 3506 cm^{-1} for O-H asymmetric stretching mode), it causes fast non-radiative relaxations, resulting in a decrease in radiative emission. As the content of H_2O_2 increases water content also increases that causes non-radiative relaxations and the radiative emission disappears. The second mechanism proposes that, the presence of H_2O_2 changes the environmental symmetry around Sm^{3+} ions and therefore emission intensity may also decrease.

The plot of emission intensity versus H_2O_2 content (figures 10(b)–(g)) for all the three emission peaks (562 nm, 602 nm and 645 nm) of Sm^{3+} also shows two clearly distinct patterns as it was observed in case of excitation. At lower contents (<22 μl), it shows a linear decay behavior while for the higher contents it shows an exponential decay behavior. The sensitivity for 562 nm, 602 nm and 645 nm peaks calculated using equation (1) for lower content region is 2.89%, 3.47% and 3.55% signal reduction per μl of H_2O_2, respectively. Thus the

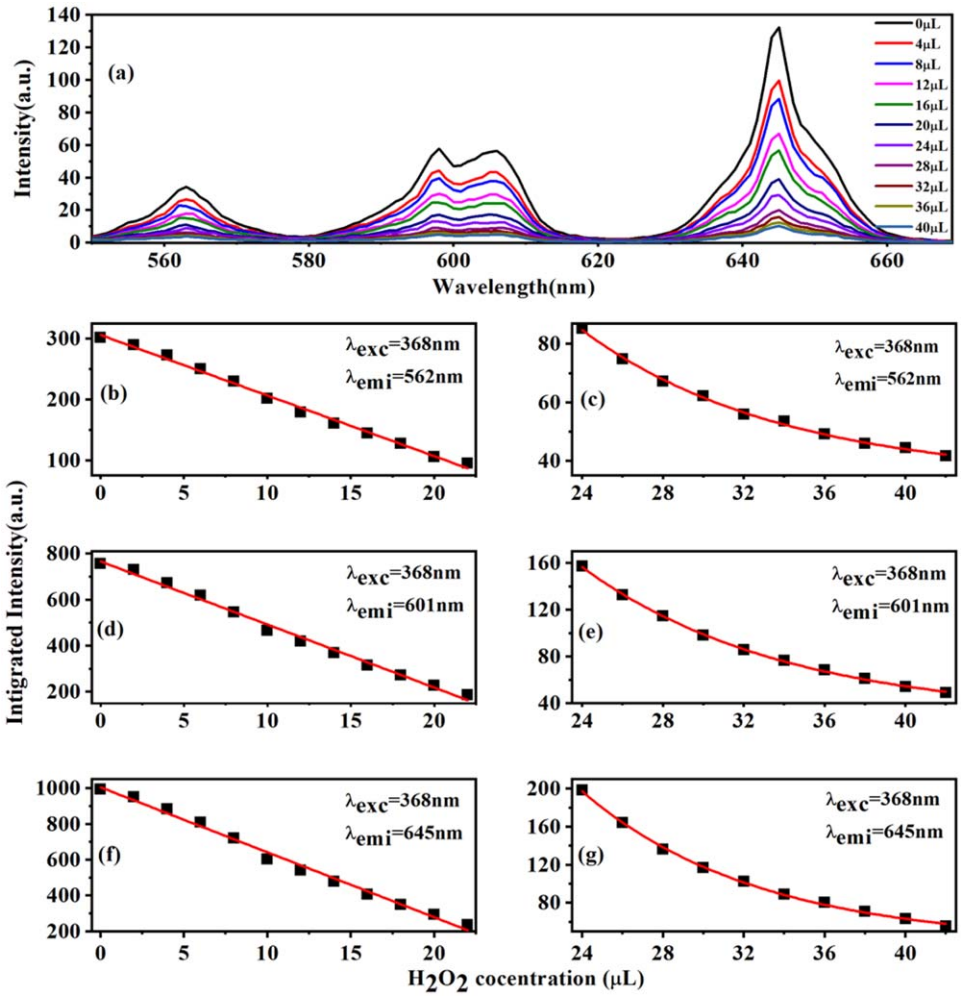

Figure 10. (a) Emission spectra of Sm^{3+} (for $\lambda_{exc} = 368$ nm) in HNPs as a function of H_2O_2 content. (b)–(g) show the emission intensity plot for 562 nm, 602 nm and 645 nm peaks as a function of H_2O_2 content in low (0–22 μl) and high content (>22 μl) range of H_2O_2. Plot shows linear decay behavior for low content while it's decay behavior is exponential for higher contents.

fluorescence quenching could be an excellent and effective way to realize H_2O_2 sensing application both through excitation and emission modes. Additionally, this technique specifies that, the content of H_2O_2 in the test sample is high or low. We also tried to probe H_2O_2 through UC emission mode. However, since UC is a non-linear process, UC emission decreases very fast and fades up at very low content of H_2O_2. This limits the use of UC mode of HNPs for sensing application of H_2O_2.

4. Conclusion

Photophysical properties, energy transfer studies and H_2O_2 sensing application have carried out using an organic-inorganic hybrid nanoparticles (HNPs) composed of $Sm(TTA)_3Phen$ and $NaY_{0.78}Er_{0.02}Yb_{0.20}F_4$. It is a dual mode emitting (both through photoluminescence and photon upconversion) and color tunable material. The HNPs shows an energy transfer from Sm^{3+} of coordination compound to Er^{3+} of inorganic NPs on exciting the material with 266 nm and 980 nm lasers simultaneously. Presence of H_2O_2 in the solution of HNPs (in cyclohexane) quenches the excitation and emission intensity of Sm^{3+} significantly. This property has been used for sensing of H_2O_2 with its specificity for lower and higher content of H_2O_2. For lower contents, the rate of decrease in emission (as well as excitation) is slow and shows a linear behavior, while it is very fast for higher contents and shows exponential behavior. The sensitivity has also been calculated for the linear region which is reasonably good. Such low cost HNPs may find vast applications in different areas ranging from sensors to photonics to biomedical.

Acknowledgments

AK acknowledges UGC, India for the award of JRF fellowship. Prof. SB Rai acknowledges UGC BSR (project no. F.18-1(84)/2015(BSR)) and Dr A Bahadur acknowledges to DST, SERB-Empowerment and Equity Opportunities for Excellence in Science scheme (File no. EEQ/2017/000757) for financial assistance.

ORCID iDs

Praveen Kumar Shahi https://orcid.org/0000-0002-4020-1187
Amresh Bahadur https://orcid.org/0000-0002-3216-9973
Sunil Kumar Singh https://orcid.org/0000-0002-1028-6255
Shyam Bahadur Rai https://orcid.org/0000-0002-6321-1038

References

[1] Deng R, Qin F, Chen R, Huang W, Hong M and Liu X 2015 Temporal full-colour tuning through non-steady-state upconversion *Nat. Nano.* **10** 237–42
[2] Wang C, Zhou T, Jiang J, Geng H, Ning Z, Lai X, Bi J and Gao D 2017 Multicolor tunable luminescence based on Tb^{3+}/Eu^{3+} doping through a facile hydrothermal route *ACS Appl. Mater. Interfaces* **9** 26184–90
[3] Wang F, Xue X and Liu X 2008 Multicolor tuning of (Ln, P)-Doped YVO4 nanoparticles by single-wavelength excitation *Angew. Chem.* **47** 906–9
[4] Liu L, Yu M, Zhang J, Wang B, Liu W and Tang Y 2015 Facile fabrication of color-tunable and white light emitting nano-composite films based on layered rare-earth hydroxides *J. Mat. Chem.* C **3** 2326–33
[5] Bedekar V, Dutta D P, Mohapatra M, Godbole S V, Ghildiyal R and Tyagi A K 2009 Rare-earth doped gadolinia based phosphors for potential multicolor and white light emitting deep UV LEDs *Nanotechnol.* **20** 125707–16
[6] Wang M, Mi C, Zhang Y, Liu J, Li F, Mao C and Xu S 2009 NIR-responsive silica-coated $NaYbF_4$: Er/Tm/Ho upconversion fluorescent nanoparticles with tunable emission colors and their applications in immune-labeling and fluorescent imaging of cancer cells *Phys. Chem.* C **113** 19021–7
[7] Boyer J C, Cuccia L A and Capobianco J A 2007 Synthesis of colloidal upconverting $NaYF_4$: Er^{3+}/Yb^{3+} and Tm^{3+}/Yb^{3+} monodisperse nanocrystals *Nano Lett.* **7** 847–52
[8] Heer S, Kömpe K, Güdel H U and Haase M 2004 Highly efficient multicolour upconversion emission in transparent colloids of lanthanide-doped $NaYF_4$ nanocrystals *Adv.Mat.* **16** 2102–5
[9] Cates E L, Cho M and Kim J H 2011 Converting visible light into UVC: microbial inactivation by Pr^{3+}-activated upconversion materials *Environ. Sci. Technol.* **45** 3680–6
[10] Zhou B, Yang W, Han S, Sun Q and Liu X 2015 Photon upconversion through Tb^{3+}-mediated interfacial energy transfer *Adv.Mat.* **27** 6208–12
[11] Wang L, Lan M, Liu Z, Qin G, Wu C, Wang X, Qin W, Huang W and Huang L 2013 Enhanced deep-ultraviolet upconversion emission of Gd^{3+} sensitized by Yb^{3+} and Ho^{3+} in β-$NaLuF_4$ microcrystals under 980 nm excitation *J. Mater. Chem.* C **1** 2485–90
[12] Auzel F 2004 Upconversion and anti-stokes processes with f and d ions in solids *Chem. Rev.* **104** 139–73
[13] Auzel F 1990 Upconversion processes in coupled ion systems *J. Lumin.* **45** 341–5
[14] Judd B R 1962 Optical absorption intensities of rare-earth ions *Phys. Revi.* **127** 750–762.
[15] Matsuura D 2002 Red, green, and blue upconversion luminescence of trivalent-rare-earth ion-doped Y_2O_3 nanocrystals *Appl. Phys. Lett.* **81** 4526–8
[16] Lu Y *et al* 2014 Tunable lifetime multiplexing using luminescent nanocrystals *Nat. Phot.* **8** 32–6
[17] Meltzer R S, Yen W M, Zheng H, Feofilov S P, Dejneka M J, Tissue B and Yuan H B 2001 Effect of the matrix on the radiative lifetimes of rare earth doped nanoparticles embedded in matrices *J. Lumi.* **94** 217–20
[18] Boyer J C, Vetrone F, Capobianco J A, Speghini A and Bettinelli M 2004 Yb^{3+} ion as a sensitizer for the upconversion luminescence in nanocrystalline $Gd_3Ga_5O_{12}$: Ho^{3+} *Chem. Phy. Lett.* **390** 403–7
[19] Mahalingam V, Vetrone F, Naccache R, Speghini A and Capobianco J A 2009 Colloidal Tm^{3+}/Yb^{3+}-doped $LiYF_4$ nanocrystals: multiple luminescence spanning the UV to NIR regions via low-energy excitation *Adv. Mat.* **21** 4025–8
[20] Gavrilović T V, Jovanović D J, Lojpur V M, Đorđević V and Dramićanin M D 2014 Enhancement of luminescence emission from $GdVO_4$: Er^{3+}/Yb^{3+} phosphor by Li^+ co-doping *J. Solid State Chem.* **217** 92–8
[21] Li X, Zhang F and Zhao D 2015 Lab on upconversion nanoparticles: optical properties and applications engineering via designed nanostructure *Chem. Soc. Rev.* **44** 1346–78
[22] Schietinger S, Menezes L D S, Lauritzen B and Benson O 2009 Observation of size dependence in multicolor upconversion in single Yb^{3+}, Er^{3+} codoped $NaYF_4$ nanocrystals *Nano Lett.* **9** 2477–81
[23] Zheng W, Huang P, Tu D, Ma E, Zhu H and Chen X 2015 Lanthanide-doped upconversion nano-bioprobes: electronic structures, optical properties, and biodetection *Chem. Soc. Rev.* **44** 1379–415
[24] Wang F, Wang J and Liu X 2010 Direct evidence of a surface quenching effect on size-dependent luminescence of upconversion nanoparticles *Angew. Chem. Int. Ed.* **49** 7456–60
[25] Li Z and Zhang Y 2008 An efficient and user-friendly method for the synthesis of hexagonal-phase NaYF4: Yb, Er/Tm nanocrystals with controllable shape and upconversion fluorescence *Nanotechnology* **19** 1–6
[26] Dong H, Sun L D and Yan C H 2015 Energy transfer in lanthanide upconversion studies for extended optical applications *Chem. Soc. Rev.* **44** 1608–34
[27] Boyer J C and Van Veggel F C 2010 Absolute quantum yield measurements of colloidal $NaYF^4$: Er^{3+}, Yb^{3+} upconverting nanoparticles *Nanoscale.* **2** 1417–9
[28] Shahi P K, Singh A K, Singh S K, Rai S B and Ullrich B 2015 Revelation of the technological versatility of the $Eu(TTA)_3Phen$ complex by demonstrating energy harvesting, ultraviolet light detection, temperature sensing, and laser applications *ACS Appl. Mater. Interfaces* **7** 18231–9

[29] Singh A K, Singh S K, Prakash R and Rai S B 2010 Structural and optical properties of $Sm(DBM)_3Phen$ doped in poly (methyl methacrylate)(PMMA): an evidence for cascading energy transfer process *Chem. Phy. Lett.* **485** 309–14
[30] Liu L *et al* 2007 Preparation and luminescence properties of $Sm(TTA)_3phen$/NBR composites *Compos. Sci. Technol.* **67** 2199–207
[31] Shahi P K, Singh A K, Rai S B and Ullrich B 2015 Lanthanide complexes for temperature sensing, UV light detection, and laser applications *Sens. Actuators A Phys.* **222** 255–61
[32] Zhang R J, Liu H G, Yang K Z, Si Z K, Zhu G Y and Zhang H W 1997 Fabrication and fluorescence characterization of the LB films of luminous rare earth complexes $Eu(TTA)_3Phen$ and $Sm(TTA)_3Phen$ *Thin Solid Films* **295** 228–33
[33] Apel K and Hirt H 2004 Reactive oxygen species: metabolism, oxidative stress, and signal transduction *Annu Rev Plant Biol.* **55** 373–99
[34] Wang S Y and Jiao H 2000 Scavenging capacity of berry crops on superoxide radicals, hydrogen peroxide, hydroxyl radicals, and singlet oxygen *J. Agric. Food Chem.* **48** 5677–84
[35] Halliwell B 1991 Reactive oxygen species in living systems: source, biochemistry, and role in human disease *Am. J. Med.* **91** 514–522.
[36] John Aitken R, Clarkson J S and Fishel S 1989 Generation of reactive oxygen species, lipid peroxidation, and human sperm function *Biol. Reprod.* **41** 183–187.
[37] Halliwell B 1992 Reactive oxygen species and the central nervous system *J. Neurochem.* **59** 1609–23
[38] Linley E, Denyer S P, McDonnell G, Simons C and Maillard J Y 2012 Use of hydrogen peroxide as a biocide: new consideration of its mechanisms of biocidal action *J. Antimicrob. Chemother.* **67** 1589–96
[39] Souza S D, J A, Ribeiro K, Teixeira A C S C, Magri N T C, Mandro J L and de Aguiar C L 2017 Sugarcane juice clarification by hydrogen peroxide: predictions with artificial neural networks *Int. J. Food Eng.* **13** 2016–0199
[40] Wang L, Zheng J, Li Y, Yang S, Liu C, Xiao Y, Li J, Cao Z and Yang R 2014 AgNP-DNA@ GQDs hybrid: new approach for sensitive detection of H_2O_2 and glucose via simultaneous AgNP etching and DNA cleavage *Anal. Chem.* **86** 12348–54
[41] Wei H and Wang E 2008 Fe_3O_4 magnetic nanoparticles as peroxidase mimetics and their applications in H_2O_2 and glucose detection *Anal. Chem.* **80** 2250–4
[42] Veal E A, Day A M and Morgan B A 2008 Hydrogen peroxide sensing and signaling *Mol. Cell.* 2007 **26** 1–14
[43] Singh P, Shahi P K, Singh S K, Singh A K, Singh M K, Prakash R and Rai S B 2016 Lanthanide doped ultrafine hybrid nanostructures: multicolour luminescence, upconversion based energy transfer and luminescent solar collector applications *Nanoscale.* **9** 696–705
[44] Shahi P K, Singh P, Singh A K, Singh S K, Rai S B and Prakash R 2017 A strategy to achieve efficient dual-mode luminescence in lanthanide-based magnetic hybrid nanostructure and its demonstration for the detection of latent fingerprints *J. Colloid Interface Sci.* **491** 199–206
[45] Cullity B D and Stock S R 2001 *Elements of x-ray diffraction* (Third Edition) 3 (New York: Prentice-Hall) P.N.I.E. Prentice-Hall
[46] Singh P, Shahi P K, Prakash R and Rai S B 2017 An assembly and interaction of upconversion, and plasmonic nanoparticles on organometallic nanofibers: enhanced multicolor upconversion, downshifting emission and the plasmonic effect *Nanotechnology* **28** 415701
[47] Pollnau M, Gamelin D R, Lüthi S R, Güdel H U and Hehlen M P 2000 Power dependence of upconversion luminescence in lanthanide and transition-metal-ion systems *Phys. Rev.* B **61** 3337–46
[48] Chen G Y, Liang H J, Liu H C, Somesfalean G and Zhang Z G 2009 Anomalous power dependence of upconversion emissions in Gd_2O_3: Er^{3+} nanocrystals under diode laser excitation of 970 nm *J. Appl. Phys.* **105** 114315
[49] Shahi P K, Kumar B, Prakash R and Rai S B 2019 Investigation of optical properties and energy transfer in Eu({III}) and Tb({III}) based composite compound dispersed in polar, non-polar solvents and polymer matrix *Mater. Res. Express* **6** 046204
[50] Shahi P K, Singh P and Rai S B 2017 Sunlight activated lanthanide complex for luminescent solar collector applications: effect of waveguide matrix *J. Phys.* D **50** 075501
[51] Lippert A R, Van de Bittner G C and Chang C J 2011 Boronate oxidation as a bioorthogonal reaction approach for studying the chemistry of hydrogen peroxide in living systems *Acc. Chem. Res.* **44** 793–804
[52] Germain M E and Knapp M J 2008 Turn-on fluorescence detection of H_2O_2 and TATP *Inorg. Chem.* **47** 9748–50